



Statistical Investigations of the Radial Interplanetary Magnetic Field Component Impact on the Magnetotail Current Sheet Structure of Mars: MAVEN Observations

Yuanzheng Wen^{1,2,7} , Zhaojin Rong^{2,3,4} , Hans Nilsson⁵ , Chi Zhang⁶ , Han-Wen Shen¹ , and Jiawei Gao⁶

¹ Department of Physics and Astronomy, The University of Iowa, Iowa City, IA, USA; yuanzheng-wen@uiowa.edu
² Key Laboratory of Planetary Science and Frontier Technology, Institute of Geology and Geophysics, Chinese Academy of Sciences, Beijing, People's Republic of China; rongzhaojin@mail.igcas.ac.cn

³ College of Earth and Planetary Sciences, University of Chinese Academy of Sciences, Beijing, People's Republic of China

⁴ Mohe Observatory of Geophysics, Institute of Geology and Geophysics, Chinese Academy of Sciences, Beijing, People's Republic of China
⁵ Swedish Institute of Space Physics, Kiruna, Sweden

⁶ Center for Space Physics and Department of Astronomy, Boston University, Boston, MA, USA

Received 2025 July 22; revised 2025 October 3; accepted 2025 October 4; published 2025 November 5

Abstract

In this study, we investigated the role of interplanetary magnetic field (IMF) orientation in controlling the location and structure of the current sheet (CS) in the Martian magnetotail. Based on carefully selected cases as well as statistical studies using the magnetic field and plasma data of Mars Atmosphere and Volatile EvolutioN from 2014 October to 2020 February, our work shows that the IMF orientation can systematically influence the magnetotail CS structure of Mars. Our results reveal a systematic dawn–dusk (Y -axis) asymmetry in CS positioning under different IMF orientations. Specifically, a sunward-directed IMF (cone angle $< 60^\circ$) shifts the CS toward the dusk ($+Y$) hemisphere, while a tailward-directed IMF (cone angle $> 120^\circ$) shifts it toward the dawn ($-Y$) hemisphere. Under cross-flow IMF conditions ($70^\circ < \text{cone angle} < 110^\circ$), no significant CS displacement is observed. This pattern persists even after accounting for possible confounding influences such as Martian crustal magnetic fields and solar EUV intensity. Our findings suggest that the cone angle of the IMF can systematically control the CS structure and magnetic lobes in the magnetotail of Mars. This IMF-controlled CS asymmetry has implications for understanding planetary ion escape and magnetotail dynamics at unmagnetized bodies.

Unified Astronomy Thesaurus concepts: Mars (1007); Solar wind (1534); Space plasmas (1544); Solar-planetary interactions (1472); Planetary science (1255); Planetary magnetospheres (997)

1. Introduction

Mars lacks a strong intrinsic magnetic field, making its interaction with the solar wind and the interplanetary magnetic field (IMF) fundamentally different from that of Earth. The solar wind interacts directly with the Martian ionosphere and upper atmosphere (A. Nagy et al. 2004; C. Bertucci et al. 2011; J. S. Halekas et al. 2021). This direct interaction induces ionospheric currents, leading to the draping and piling up of the IMF around the planet, which forms an induced magnetosphere. Mass loading from ionized atmospheric heavy ions slows and deflects the solar wind flow, further shaping the structure of the Martian induced magnetosphere. Consequently, a distinct magnetotail structure forms, consisting of two magnetic lobes separated by a central current sheet (CS) with antiparallel magnetic field lines on either side (E. Dubinin & M. Fraenz 2015). The induced magnetotail is highly dynamic in terms of its position, structure, and plasma compositions (M. W. Liemohn & S. Xu 2018; X. Li et al. 2023; C. Zhang et al. 2024, 2025; Y. Wen et al. 2025a), and it serves as a critical channel for ion escape (H. Nilsson et al. 2010; E. Dubinin et al. 2012; Y. Dong et al. 2015, 2017; H.-W. Shen et al. 2024). Additionally, Mars has localized

crustal magnetic fields (M. Acuna et al. 1999), particularly concentrated in the southern hemisphere, which add further complexity to its magnetospheric structure and plasma dynamics (Y. Ma et al. 2002; D. A. Brain et al. 2003; E. Dubinin et al. 2023). Understanding the structure and variability of the Martian magnetotail is therefore essential for accurately characterizing ion escape processes and assessing the long-term evolution of the planet's atmosphere (D. A. Brain et al. 2017).

Early observations of Venus' magnetotail using data from the Pioneer Venus Orbiter (PVO) revealed a consistent dawn–dusk ($\pm Y$) asymmetry in the CS position relative to the planet (D. J. McComas et al. 1986). Through a statistical analysis of magnetic field (B) measurements, D. J. McComas et al. (1986) found that the average CS center is displaced by approximately $0.5 R_V$ toward the $+B_X$ hemisphere, where R_V denotes Venus radii and X is the flow-aligned (radial) component. They reported that the magnetic field angle (computed as $\text{atan}(B_X/B_Y)$) in the lobes differed significantly: -78.4° in the $-B_X$ hemisphere and 73.4° in the $+B_X$ hemisphere. The transverse lobe widths were estimated to be 2.1 and $1.6 R_V$, respectively, and the $-B_X$ hemisphere exhibited a stronger B_X component. These patterns were interpreted as evidence that the flow-aligned component of the IMF modulates the magnetic field draping and tension balance in the magnetotail, thereby displacing the tail CS. This hypothesis was later supported by magnetohydrodynamic (MHD) simulations (Y. Ma et al. 2013). However, subsequent Venus Express (VEX) observations questioned this interpretation, showing little sensitivity of the near-Venus magnetotail CS

⁷ The first author, Yuanzheng Wen, finished this work at the Chinese Academy of Sciences in 2021 and has joined the University of Iowa as a Ph.D. student since 2023 August.



Original content from this work may be used under the terms of the [Creative Commons Attribution 4.0 licence](#). Any further distribution of this work must maintain attribution to the author(s) and the title of the work, journal citation and DOI.

displacement to the IMF B_X (Z. Rong et al. 2016), leaving the origin of the asymmetry unresolved.

Similar displacements of the magnetotail CS have also been observed at other unmagnetized bodies in the solar system. At Titan, both hybrid simulations (S. Simon & U. Motschmann 2009) and in situ observations from Cassini flybys (S. Simon et al. 2013) revealed a strong correlation between the CS location and the magnetic field aligned with Saturn’s corotational flow. At Mars, J. S. Halekas et al. (2006) found many CS crossings in upper ionospheric magnetic data at 2 A.M. local time using Mars Global Surveyor (MGS) data, implying a systematic $-Y$ shift in the magnetotail CS, while G. A. DiBraccio et al. (2015) documented a positive Y displacement in a near-tail case. Further analysis by N. Romanelli et al. (2015) using a limited data set from MGS found that the structure of the Martian magnetotail lobes correlates with the orientation of the IMF, consistent with earlier results for Venus by D. J. McComas et al. (1986). However, several constraints in N. Romanelli et al. (2015) still leave open questions, most notably, the relatively sparse data coverage (only 71 orbits), lack of direct plasma measurements, and the absence of a quantitative assessment of the CS displacement or its variability across a broader range of IMF conditions. These limitations cast uncertainty on the generalizability and robustness of their conclusions. More recent work by C. Zhang et al. (2022) identified the formation of an inverse polarity reversal layer (IPRL) in the Martian magnetotail under strong IMF B_X conditions and its shift with respect to the IMF orientation using over 6 yr of Mars Atmosphere and Volatile EvolutioN’s (MAVEN) data. Additionally, G. Li et al. (2023) used MHD simulations to demonstrate CS displacement and lobe asymmetry in response to different Parker spiral angles, further highlighting the influence of IMF orientation. Despite these advances, the specific role of the IMF B_X component in shaping the structure of Mars’ magnetotail and CS location remains poorly constrained by direct observations. A more comprehensive analysis using multi-instrument data from the MAVEN mission is, therefore, necessary to clarify its impact.

In this study, we aim to investigate the influence of IMF orientation—specifically the IMF cone angle, defined as the angle between the IMF vector and the solar wind velocity vector—on the structure of the Martian magnetotail CS with improved accuracy. Using data from the MAVEN mission (2014 October–2020 February), we focused on cases with minimal upstream IMF variability to isolate the effects of other contributing factors. Additionally, we evaluated the role of crustal magnetic fields and other influences on magnetotail configurations, comparing their relative contributions. The structure of the paper is as follows: Section 2 introduces the instruments and datasets used; Section 3 outlines the quantitative analysis techniques applied to evaluate CS displacement. Results from case studies are presented in Section 4, followed by statistical analyses in Section 5. Finally, Section 6 summarizes the findings, discusses their implications, and provides conclusions.

2. Instrumentation and Dataset

The MAVEN spacecraft was inserted into orbit around Mars on 2014 September 21 and began its primary science phase on 2014 November 16 following a brief commissioning period. MAVEN operates in a 4.5 hr elliptical orbit, with periapsis and apoapsis altitudes of approximately 150 and 6200 km,

respectively. Its 74° inclination allows for comprehensive coverage of the Martian space environment, enabling sampling across a wide range of latitudes and local times throughout the mission’s orbital evolution (B. M. Jakosky et al. 2015).

This study utilizes magnetic field, ion, and electron measurements from MAVEN to identify CS crossing events. The magnetometer (MAG) provides high-resolution vector magnetic field data at up to 32 vectors per second (J. Connerney et al. 2015). The Solar Wind Ion Analyzer (SWIA) delivers three-dimensional ion distributions in the 25 eV–25 keV energy range and computes ion moments at a cadence of 4 s (J. S. Halekas et al. 2015). The Solar Wind Electron Analyzer (SWEA) records electron energy spectra and pitch angle distributions with a 2 s temporal resolution (D. Mitchell et al. 2016). The Suprathermal and Thermal Ion Composition (STATIC) instrument, featuring an electrostatic top-hat analyzer combined with a time-of-flight velocity analyzer, detects ions from 0.1 eV to 30 keV over a $360^\circ \times 90^\circ$ field of view. It also enables mass-resolved ion identification with a 4 s cadence (J. McFadden et al. 2015). From the three-dimensional ion distributions, detailed moments—including density, temperature, and velocity—for key species such as H^+ , O^+ , and O_2^+ are derived (K. G. Hanley et al. 2021; C. Fowler et al. 2022).

3. Analysis Technique

3.1. The Normal of the Current Sheet

To study the CS structure in the Martian magnetotail, determining the normal direction (\hat{n}) to the CS is essential. The minimum variance analysis (MVA) method (B. U. Sonnerup 1998) is applied to the MAG data for individual CS encounters to derive this normal direction. Considering the boundary condition $B_{1n} = B_{2n}$ at the magnetic discontinuity (due to $\nabla \cdot \mathbf{B} = 0$), where B_{1n} and B_{2n} are the normal components of the magnetic field on either side of the discontinuity, the normal direction \hat{n} is determined by minimizing the variance:

$$\sigma^2 = \frac{1}{N} \sum_{i=1}^N |(\mathbf{B}_i - \langle \mathbf{B} \rangle) \cdot \hat{n}|^2. \quad (1)$$

Here, $\langle \mathbf{B} \rangle = \frac{1}{N} \sum_{i=1}^N \mathbf{B}_i$ and $i = 1, 2, 3 \dots N$. N is the number of data points. Using the MVA, a local Cartesian coordinate system, $\{X_1, X_2, X_3\}$ is established for each CS. These axes correspond to the orthogonal eigenvectors derived from the magnetic variance matrix $M_{\mu\nu} = \langle B_\mu B_\nu \rangle - \langle B_\mu \rangle \langle B_\nu \rangle$, where the subscripts $\mu, \nu = 1, 2, 3$ represent the Cartesian components along the X, Y, Z coordinate system. The eigenvectors (X_1, X_2, X_3) are associated with the eigenvalues $\lambda_1, \lambda_2, \lambda_3 (\lambda_1 \geq \lambda_2 \geq \lambda_3 \geq 0)$, where $X_3 = X_1 \times X_2$.

The angular uncertainty of these eigenvectors can be estimated as

$$|\Delta \varphi_{ij}| = |\Delta \varphi_{ji}| = \sqrt{\frac{\lambda_3(\lambda_i + \lambda_j - \lambda_3)}{(N-1)(\lambda_i - \lambda_j)^2}}. \quad (2)$$

Here $|\Delta \varphi_{ij}|$ represents the angular uncertainty of eigenvector X_i for rotation toward or away from eigenvector X_j , while N is the number of data points.

The eigenvectors X_1, X_2, X_3 are commonly referred to as $\hat{L}, \hat{M}, \hat{N}$ to represent the direction of maximum, intermediate, and minimum variance of the magnetic field, respectively. The minimum variance direction \hat{N} is considered the normal to the

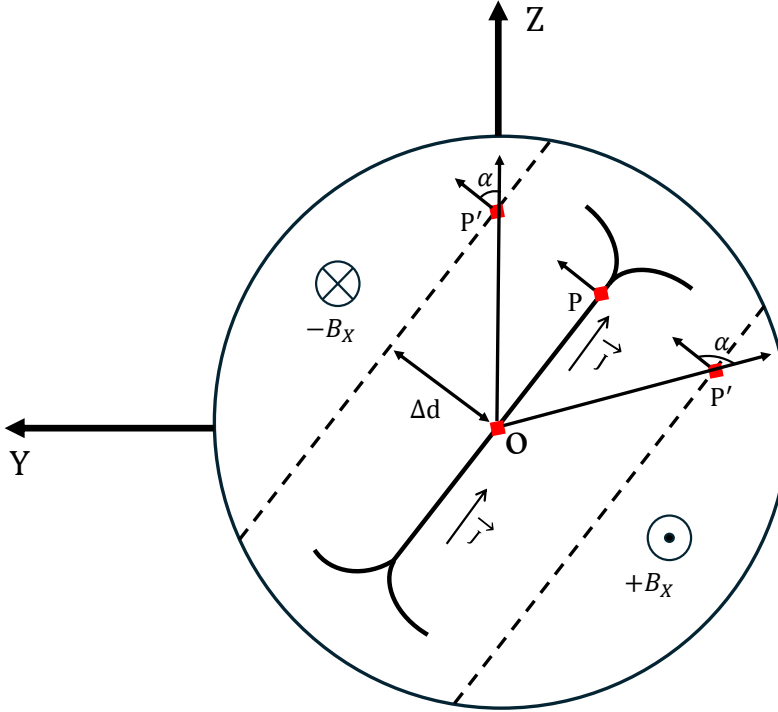


Figure 1. Diagram illustrating the method used to estimate the shift of the CS. The unshifted CS is shown as a thick black line, while the CS crossing observed by MAVEN is marked as point P . Thin dashed black lines represent possible configurations of a displaced CS, with corresponding crossing points labeled as P' . The CS normal vector, denoted as \hat{n} , consistently points from the $+B_X$ hemisphere to the $-B_X$ hemisphere. The deviation angle α , defined between vector OP' and \hat{n} , exceeds 90° when the CS is significantly displaced toward the $+B_X$ hemisphere and is less than 90° when displaced toward the $-B_X$ hemisphere. Figure adapted from Z. Rong et al. (2016) and G. A. DiBraccio et al. (2017).

CS. The reliability of the MVA results is inferred from the eigenvalue ratios, particularly the intermediate-to-minimum eigenvalue ratio (λ_2/λ_3). A higher λ_2/λ_3 ratio (>3) indicates better determination of the CS normal (B. U. Sonnerup 1998; G. A. DiBraccio et al. 2015; Z. Rong et al. 2015a, 2016). For further analysis, the normal vector \hat{n} is defined to always point from the $+B_X$ to the $-B_X$ hemisphere. This is achieved using the following formulation:

$$\hat{n} = \text{sgn}(-\Delta B_X) \cdot \text{sgn}(\hat{v}_t \cdot \hat{N}) \hat{N}, \quad (3)$$

where sgn is the sign function, \hat{v}_t represents the velocity vector of MAVEN, and $\Delta B_X > 0$ if B_X changes from $-B_X$ to $+B_X$, and vice versa.

3.2. Current Sheet Structure Shift Evaluation

To investigate the relationship between the IMF cone angle and the displacement of the CS structure, it is essential to quantitatively estimate the CS shift under varying IMF orientations.

We adopt and extend the technique introduced by Z. Rong et al. (2016) to perform this analysis. In this approach, the CS is modeled as an ideal planar structure, with the solar wind assumed to flow along the $-X$ direction. As illustrated in Figure 1 (projected onto the YZ plane), a perfectly centered and unshifted CS would align with the Sun–Mars line, represented by the thick black line. In this symmetric configuration, the CS intersects the origin point O , corresponding to the equatorial center of the CS, and the magnetic lobes on either side, $+B_X$ and $-B_X$ hemispheres, would be balanced in size.

If the CS is shifted toward either lobe, as indicated by the dashed black lines, the symmetry is broken, and the spacecraft crossing occurs at a shifted location denoted as P' . The position of P' provides a geometric proxy for the CS displacement. When no significant shift occurs, the deviation angle α between the CS normal vector \hat{n} and the position vector (OP or OP') is approximately 90° . A displacement toward the $+B_X$ hemisphere yields $\alpha > 90^\circ$, while a shift toward the $-B_X$ hemisphere results in $\alpha < 90^\circ$.

The magnitude of the CS shift is quantified by the projected distance $\Delta d = |OP'| \cos \alpha$. This formulation remains valid even when the CS normal vector has a significant n_X component. In such cases, the cross-flow component of the normal vector, $\hat{n}_{\perp} = (0i, n_yj, n_zk)$, is used to compute α . Notably, this method does not rely on concurrent upstream IMF measurements, enabling estimation of CS displacement in data intervals without simultaneous solar wind observations. Moreover, incorporating the angular uncertainty of the CS normal vector (as described in Equation (2)) allows for corresponding uncertainty estimation in Δd .

4. Case Studies

To systematically evaluate the potential influence of the IMF flow-aligned component (cone angle) on the CS structure, we begin by examining three representative cases. These cases are selected to highlight varying IMF flow directions, including one with a significant sunward flow component, another with a dominant cross-flow component, and a third one with a dominant tailward flow component. This comparative approach provides insights into how different IMF orientations may impact the CS structure.

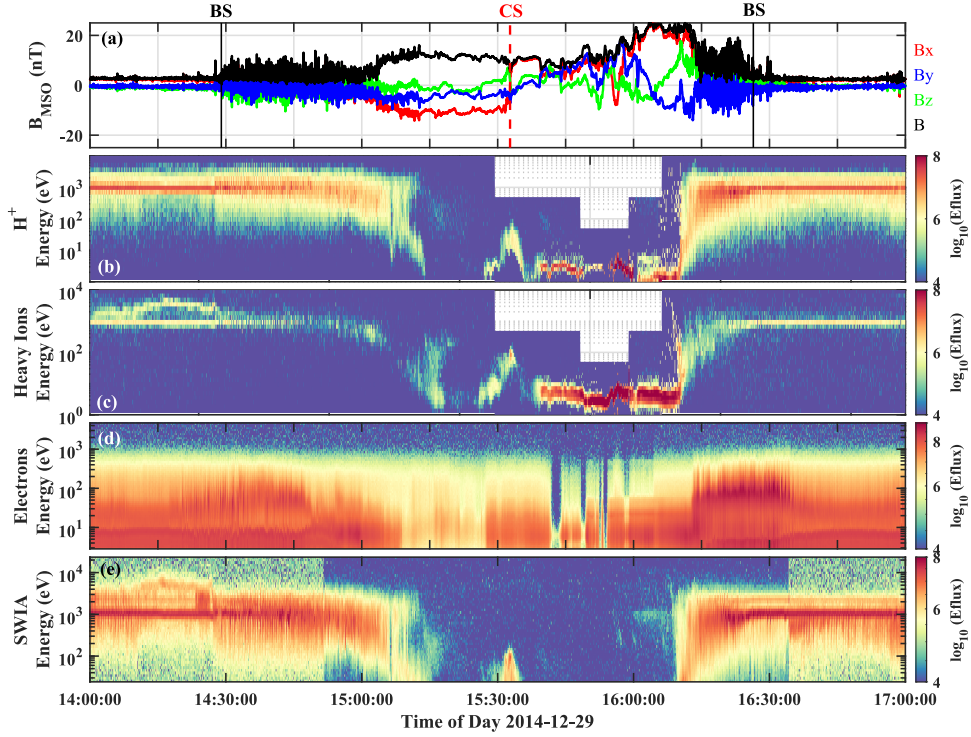


Figure 2. MAVEN crossing of the Martian induced magnetosphere on 2014 December 29. The time series of the magnetic field in MSO coordinates, the energy–time spectrogram of ions, electrons, and solar wind ions. The crossings of the bow shock and the tail CS are labeled by vertical black and red dashed lines, respectively.

4.1. Case on 2014 December 29

As shown in Figure 2, MAVEN traversed the Martian induced magnetosphere between 14:00 and 17:00 UTC on 2014 December 29. The time-series data from MAG, STATIC, SWEA, and SWIA are displayed in the figure, including the magnetic field and its three components in Mars-Solar-Orbital (MSO) coordinates, where the X-axis points from the center of Mars to the Sun, the Z-axis points to the north pole of Mars’s orbital plane, and the Y-axis completes the right-handed orthogonal coordinate system, as well as the energy–time spectrograms of electrons (SWEA) and ions (STATIC and SWIA).

MAVEN’s crossings of the bow shock are indicated by vertical black lines in Figure 2, characterized by sharp gradients in multiple parameters. As MAVEN enters the magnetosheath from the upstream solar wind, a typical signature is the broadening of the ion energy spectrum, indicative of ion deceleration and collisionless thermalization at the shock front. This transition is also accompanied by a drop in ion bulk velocity, an increase in ion density, and an enhancement in both the magnetic field magnitude and its fluctuations relative to upstream conditions (J. S. Halekas et al. 2017; D. Liu et al. 2021; J. Fruchtman et al. 2023; H.-W. Shen et al. 2025). The average IMF 30 minutes before the inbound bow shock crossing was $B_1 = [2.52, -0.90, -0.48]$ nT, while the average IMF after the outbound bow shock crossing was $B_2 = [2.34, -0.22, -0.84]$ nT. The average IMF during the magnetospheric traversal was calculated as $(B_1 + B_2)/2 = [2.43, -0.56, -0.66]$ nT, with a cone angle of 19° . This indicates a predominantly sunward orientation of the IMF, dominated by the $+B_X$ component. Additionally, the IMF remained relatively steady before and after the bow shock crossings (as per the definition of steady IMF in Section 4.4).

The CS crossing occurred at 15:32:44 UTC, marked by the red dashed vertical line in Figure 2, when MAVEN was located at $[-1.07, 0.74, -0.16] R_M$, where R_M denotes Mars radii. The crossing was identified by a reversal in the B_X component, changing from tailward to sunward, and was accompanied by enhancements in both electron and ion fluxes (J. S. Halekas et al. 2006; E. Dubinin & M. Fraenz 2015; X. Li et al. 2023), confirming that MAVEN crossed the CS in the magnetotail. It should be noted that in the upstream solar wind and magnetosheath, background contamination is present in the heavy ion channels due to internal scattering of solar wind protons (Figure 2(c)). This appears as narrow bands at the solar wind energy level in the heavy ion spectra (Y. Dong et al. 2015; J. McFadden et al. 2015; J. S. Halekas et al. 2018). Because our analysis of the CS displacement relies exclusively on magnetic field data, this background does not affect the subsequent analysis and results, and we therefore make no effort to remove it.

Figure 3 illustrates MAVEN’s trajectory during the interval from 14:00 to 17:00 UTC. Figure 3(a) provides a meridional plane view, while Figure 3(b) presents a tailward perspective of the planet, and Figure 3(c) is in cylindrical coordinates. Red stars mark the CS crossing location. As described in Section 3.1, the MVA technique was applied to magnetic field data collected during the CS crossing from 15:31:52 to 15:33:36 UTC to determine the CS normal direction. The MVA yielded the following results for the magnetic field variance directions $\hat{L} = [0.86, -0.51, 0.009]$, $\hat{M} = [-0.17, -0.30, -0.94]$, and $\hat{n} = [0.48, 0.80, -0.35]$. The corresponding eigenvalues were $\lambda_1 = 51.2$, $\lambda_2 = 1.22$, and $\lambda_3 = 0.31$. Applying the analysis technique introduced in Section 3.2, the shift of the CS structure is quantitatively analyzed by calculating the angle, α , between the n_\perp and the position of

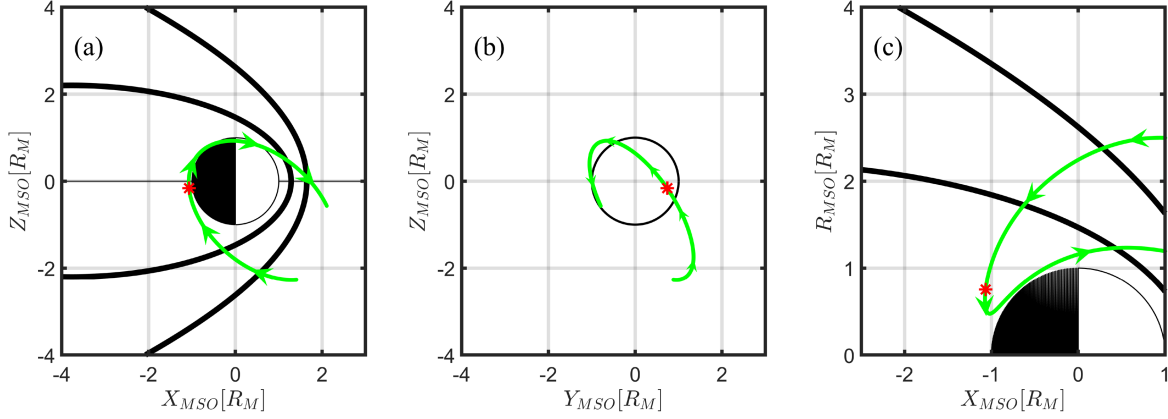


Figure 3. MAVEN trajectory on 2014 December 29, shown in three projections: (a) X - Z plane, (b) Y - Z plane, and (c) X - R plane, where $R = \sqrt{Y^2 + Z^2}$. In panels (a) and (c), the nominal bow shock (BS) and induced magnetosphere boundary (IMB) are shown as black lines based on the model by D. Vignes et al. (2000). The red star marks the location of the CS crossing.

Table 1
The Parameters Related to the Current Sheet Crossing Cases

Time	Location ^a (R_M)	IMF ^b	Cone Angle ^b (deg)	\hat{n}	λ_2/λ_3	Δd^c
2014/12/29 15:32:44	(−1.07, 0.74, −0.16)	(2.43, −0.56, −0.66)	20	(0.48, 0.79, −0.35)	3.92	+0.73 ∈ [0.72, 0.74]
2015/09/03 21:52:51	(−1.19, −0.42, −0.38)	(−3.10, 6.52, 0.19)	115	(−0.11, 0.73, −0.68)	10.81	−0.05 ∈ [−0.08, −0.02]
2016/02/02 11:02:04	(−1.00, −0.82, −0.31)	(−4.73, 0.61, 1.73)	159	(0.33, 0.85, 0.42)	5.40	−0.87 ∈ [−0.88, −0.87]

Notes.

^a The location of the current sheet crossing in MSO coordinates.

^b The averaged IMF and its cone angle.

^c The shifted distance of the current sheet plane. The sign “−” (+) represents that the current sheet is shifted toward the $+B_X$ ($-B_X$) hemisphere, and vice versa. The range of the shifted distance is shown in the square bracket.

the observed CS crossing position vector. The angle was calculated as $\alpha \approx 11^\circ$, and the CS shift distance was estimated as $\Delta d \approx 0.73R_M$, indicating a significant displacement of the CS structure toward the $-B_X$ hemisphere. The MVA results' reliability, inferred from the intermediate-to-minimum eigenvalue ratio ($\lambda_2/\lambda_3 = 3.9$), confirms that the CS normal direction was well-determined (B. U. Sonnerup 1998; Z. Rong et al. 2015a, 2016). The distance of the crossing location from the equatorial plane was estimated to be $R \approx 0.75R_M$. Considering the angular uncertainty of \hat{n} relative to \hat{M} , the range of the CS shift distance was estimated as $\Delta d \in [0.72, 0.74]R_M$. The parameters corresponding to these crossings are summarized in Table 1.

4.2. Case on 2015 September 3

Another representative event occurred on 2015 September 3, under conditions dominated by the cross-flow component of the IMF, as shown in Figure 4. The inbound and outbound bow shock crossings, indicated by vertical black lines, were observed at 21:05:07 and 23:39:51 UTC, respectively. These crossings are characterized by magnetic field fluctuations and enhancements in ion energy flux. The 30 minute average IMF prior to the inbound crossing was $\mathbf{B}_1 = [-2.84, 6.22, 0.27]$ nT, and the postoutbound average was $\mathbf{B}_2 = [-3.36, 6.83, 0.11]$ nT. The mean IMF over the full magnetospheric traversal was $(\mathbf{B}_1 + \mathbf{B}_2)/2 = [-3.10, 6.52, 0.19]$ nT, corresponding to a cone angle of 115° . These values confirm that the IMF during this event was primarily oriented in the cross-flow direction, with a stable B_X component.

The CS crossing occurred at 21:52:51 UTC, marked by the vertical red dashed line in Figure 4. At this time, MAVEN was located at $[-1.19, -0.42, -0.38]R_M$. The CS crossing was identified by a reversal in the B_X component—from tailward to sunward—accompanied by enhanced ion and electron fluxes, as observed by the SWIA and SWEA instruments. MAVEN's trajectory during this interval is shown in Figure 5, with the CS crossing indicated by red stars.

The MVA was performed on the magnetic field data between 21:52:31 and 21:53:11 UTC. The resulting eigenvectors were $\hat{L} = [0.98, 0.22, 0.08]$, $\hat{M} = [-0.21, 0.65, 0.73]$, and $\hat{n} = [-0.11, 0.73, -0.68]$, with corresponding eigenvalues $\lambda_1 = 11.4$, $\lambda_2 = 0.0893$, and $\lambda_3 = 0.00826$.

Using the same technique described in Section 3.2, the position of the CS crossing relative to the equatorial center of the CS plane was estimated to be $R \approx 0.57R_M$. The deviation angle between the CS normal vector and the position vector was $\alpha \approx 95^\circ$. This yielded a calculated CS displacement of $\Delta d \approx -0.05R_M$, suggesting that under cross-flow-dominated IMF conditions, the CS remains relatively symmetric, with minimal displacement toward the $+B_X$ hemisphere. When accounting for angular uncertainty via Equation (2), the estimated range of displacement was $\Delta d \in [-0.08, -0.02] R_M$.

4.3. Case on 2016 February 2

Figure 6 presents a representative case in which the dominant IMF B_X component strongly controls the magnetotail configuration. The vertical black lines denote the times of MAVEN's inbound and outbound bow shock crossings. The

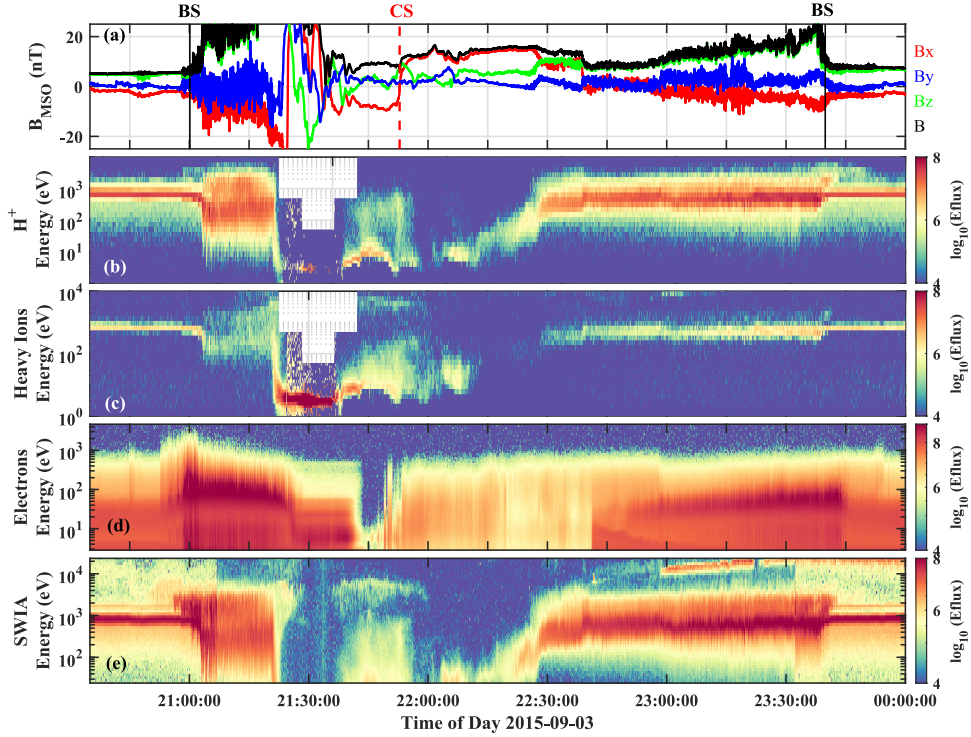


Figure 4. MAVEN crossing of the Martian induced magnetosphere on 2015 September 3. The time series of the magnetic field in MSO coordinates, the energy–time spectrogram of ions, electrons, and solar wind ions. The position of MAVEN in MSO is given below the panels. The crossings of the bow shock and the tail CS are labeled by vertical black and red dashed lines, respectively.

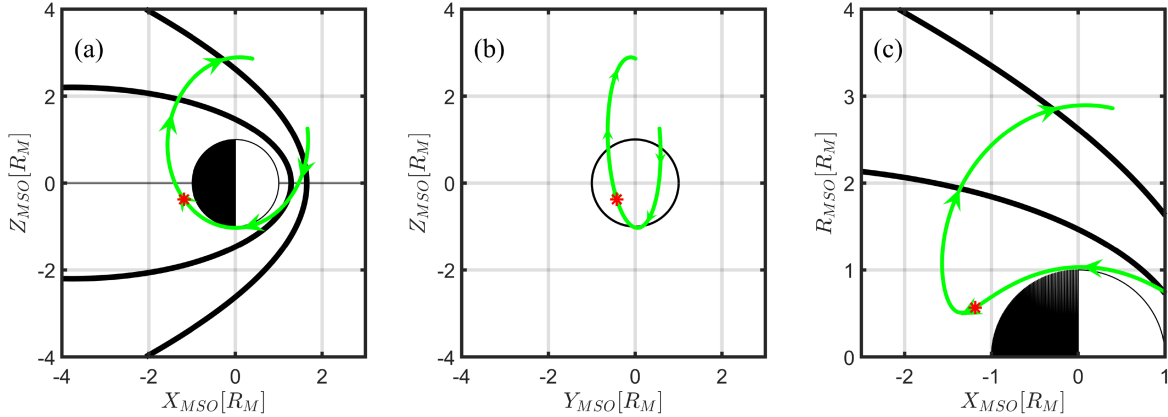


Figure 5. MAVEN's trajectory on 2015 September 3. The format is the same as Figure 3.

30 minute averaged IMF vector prior to the inbound crossing was $\mathbf{B}_1 = [-4.06, -0.15, 2.68]$ nT, while the postoutbound average was $\mathbf{B}_2 = [-5.40, 1.36, 0.78]$ nT. The mean IMF during the magnetospheric traversal, calculated as $(\mathbf{B}_1 + \mathbf{B}_2)/2 = [-4.73, 0.61, 1.73]$ nT, corresponded to a cone angle of 159°, confirming a strongly tailward-aligned IMF orientation throughout the interval.

The CS crossing was identified at 11:02:04 UTC, indicated by the vertical red line, when MAVEN was located at $[-1.00, 0.82, -0.31]R_M$ as shown in Figure 7. Due to the unavailability of SWEA data for this event, only ion energy spectrograms are shown. The CS crossing was determined based on a clear reversal in the B_X component of the magnetic field, coincident with ion energization. The MVA was applied to magnetic field data within the interval 11:01:28–11:02:40 UTC, yielding the following eigenvectors: $\hat{\mathbf{L}} = [-0.93, 0.22, 0.29]$,

$\hat{\mathbf{M}} = [0.15, -0.48, 0.86]$, and $\hat{\mathbf{n}} = [0.85, 0.33, 0.42]$, with corresponding eigenvalues $\lambda_1 = 2.50$, $\lambda_2 = 0.79$, and $\lambda_3 = 0.15$. The deviation angle α between the cross-flow component of the CS normal, $\hat{\mathbf{n}}_{\perp}$, and the spacecraft position vector was found to be 174°. Based on this angle, the CS displacement was estimated as $\Delta d \approx -0.87 R_M$, indicating a substantial shift of the CS toward the $+B_X$ hemisphere under the influence of the tailward IMF. Considering the angular uncertainty of $\hat{\mathbf{n}}$ relative to $\hat{\mathbf{M}}$, the resulting uncertainty range for the displacement was $\Delta d \in [-0.88, -0.87]R_M$.

4.4. More Cases

To systematically investigate whether the flow-aligned IMF component affects the CS structure and contributes to the asymmetry in the Martian magnetotail, additional CS crossing cases were selected for analysis. This study utilized MAVEN

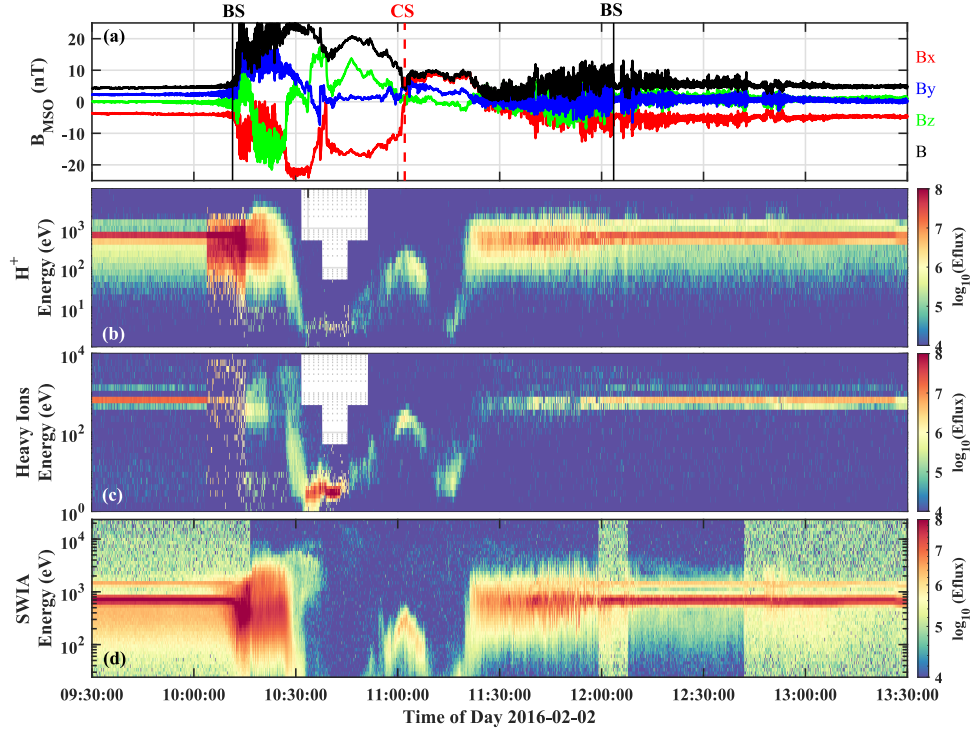


Figure 6. MAVEN crossing of the Martian induced magnetosphere on 2016 February 2. The time series of the magnetic field in MSO coordinates, the energy-time spectrogram of ions and solar wind ions. The position of MAVEN in MSO is given below the panels. The crossings of the bow shock and the tail CS are labeled by vertical black and red dashed lines, respectively.

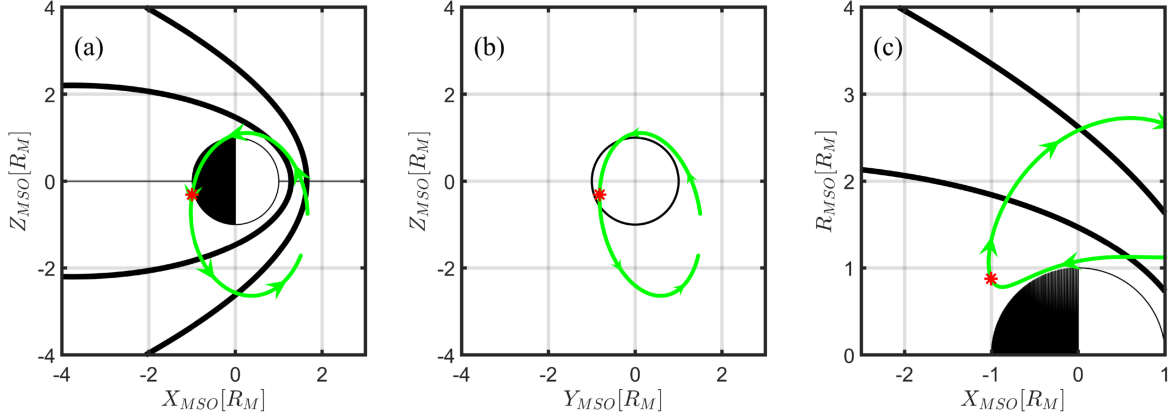


Figure 7. MAVEN's trajectory on 2016 February 2. The format is the same as Figure 3.

magnetic field data with a 1 s time resolution, collected between 2014 October and 2020 February. The selection criteria for identifying suitable CS crossings were as follows:

1. *Magnetotail location.* Events were restricted to intervals when MAVEN was located within the Martian magnetotail, defined by $-3R_M < X < -0.5R_M$ and cylindrical radial distance $\rho = \sqrt{Y^2 + Z^2} < 1.3R_M$.

2. *Current sheet identification.* CS crossings were visually identified by a reversal in the B_X component of the magnetic field, accompanied by enhancements in both ion and electron fluxes (J. S. Halekas et al. 2006; E. Dubinin & M. Fraenz 2015; X. Li et al. 2023). To ensure a quasi-static structure, only events with no apparent CS flapping signatures (Z. Rong et al. 2015b; G. A. DiBraccio et al. 2017; C. Zhang et al. 2023; Y. Wen et al. 2025a) were selected. Additionally, only single-crossing events were

included per magnetotail traversal to enable robust structural analysis.

3. *Steady IMF conditions.* To ensure stable upstream solar wind conditions, the average IMF was computed using 30 minute intervals before the inbound bow shock crossing (\mathbf{B}_1) and after the outbound crossing (\mathbf{B}_2). The average upstream IMF was defined as $(\mathbf{B}_1 + \mathbf{B}_2)/2$. Steadiness was assessed following established criteria: the deviation angle α between \mathbf{B}_1 and \mathbf{B}_2 had to be less than 30° , and the relative strength variation had to satisfy $\frac{2||\mathbf{B}_1 - \mathbf{B}_2||}{||\mathbf{B}_1 + \mathbf{B}_2||} < 0.2$ (Z. Rong et al. 2014, 2015b, 2016; Y. Ding & Z. Rong 2018). A complete list of MAVEN bow shock crossings between 2014 October and 2020 February is provided in Y. Wen (2025).

4. *Visual inspection for IMF fluctuations.* Events exhibiting significant IMF variability within 30 minutes before or after

Table 2
The Table Format Is the Same as Table 1 with More Current Sheet Crossing Cases

Time	Location ^a (R_M)	IMF ^b	Cone Angle ^b (deg)	\hat{n}	λ_2/λ_3	Δd^c
2014/12/29 15:32:44	(−1.07, 0.74, −0.16)	(2.43, −0.56, −0.66)	20	(0.48, 0.79, −0.35)	3.92	+0.73 ∈ [0.72, 0.74]
2016/08/15 20:30:25	(−1.10, −0.12, 0.37)	(3.28, 0.70, 1.31)	24	(−0.35, −0.67, 0.65)	15.52	+0.34 ∈ [0.34, 0.35]
2014/12/22 09:28:21	(−1.21, 0.55, −0.15)	(2.77, −3.24, −3.20)	59	(−0.03, 0.97, −0.24)	11.91	−0.57 ∈ [−0.56, −0.58]
2015/08/31 20:01:48	(−1.17, −0.49, −0.34)	(0.47, 4.43, −0.98)	84	(0.22, −0.47, −0.85)	10.28	+0.53 ∈ [0.52, 0.55]
2015/09/29 09:09:28	(−1.55, 0.14, −0.41)	(0.23, 2.19, −0.06)	84	(−0.01, 0.40, −0.92)	11.59	+0.43 ∈ [0.420, 0.432]
2018/04/03 11:23:17	(−1.33, 0.15, −0.4)	(−0.19, −2.13, −0.06)	95	(−0.23, −0.37, −0.90)	8.17	−0.43 ∈ [−0.4, 0.43]
2014/12/04 06:00:12	(−1.47, 0.05, −0.25)	(−0.58, 3.47, −1.56)	99	(0.18, 0.45, −0.88)	1.64	+0.25 ∈ [0.23, 0.25]
2017/07/09 19:53:59	(−1.32, 1.08, −1.52)	(−3.10, 6.52, 0.19)	103	(−0.29, −0.93, 0.23)	4.47	−0.68 ∈ [−0.85, −0.43]
2015/09/03 21:52:51	(−1.19, −0.42, −0.38)	(−3.10, 6.52, 0.19)	115	(−0.11, 0.73, −0.68)	10.81	−0.05 ∈ [−0.08, −0.02]
2014/12/05 09:40:14	(−1.30, −0.10, 0.13)	(−3.84, 2.98, −0.87)	141	(0.23, 0.97, −0.09)	5.33	−0.11 ∈ [−0.12, −0.10]
2018/03/14 12:41:51	(−1.17, −0.40, −0.39)	(−2.04, 1.41, 0.53)	144	(0.17, 0.91, −0.37)	10.71	−0.22 ∈ [−0.25, −0.20]
2018/02/19 00:47:08	(−0.68, −1.12, −0.20)	(−1.94, −0.63, 1.24)	145	(0.12, 0.18, 0.98)	3.95	−0.40 ∈ [−0.50, −0.29]
2016/03/05 03:56:42	(−1.20, −0.12, 0.48)	(−1.34, −0.29, −0.59)	154	(−0.73, 0.1, −0.68)	9.31	−0.87 ∈ [−0.88, −0.87]
2016/02/02 11:02:04	(−1.00, −0.82, −0.31)	(−4.73, 0.61, 1.73)	159	(0.33, 0.85, 0.42)	5.40	−0.11 ∈ [−0.12, −0.10]

Notes.^a The location of the current sheet crossing in MSO coordinates.^b The averaged IMF and its cone angle.^c The shifted distance of the current sheet plane. The sign “−” (+) represents that the current sheet is shifted toward the $+B_X$ ($-B_X$) hemisphere, and vice versa. The range of the shifted distance is shown in the square brackets.

the bow shock crossings were excluded to ensure the integrity of upstream IMF characterization.

5. *Exclusion of crustal magnetic field influence.* To minimize the impact of Martian crustal magnetic fields, we adopted a quantitative filter requiring the observed magnetic field strength to exceed the modeled crustal field strength by 1 order of magnitude: $|B_{\text{obs}}| > 10|B_{\text{model}}|$, where $|B_{\text{model}}|$ is derived from the spherical harmonic crustal field model of J. Gao et al. (2021). However, we acknowledge that this criterion may not entirely eliminate indirect effects of crustal fields on solar wind–magnetosphere interaction processes such as magnetic reconnection (G. A. DiBraccio et al. 2018; Y. Harada et al. 2018; C. Zhang et al. 2022).

Using the selection criteria described above, 14 CS crossing events were identified for detailed analysis. The relevant parameters for these events are summarized in Table 2. Based on this dataset, Figure 8 illustrates the relationship between the CS displacement distance (Δd) and the upstream IMF cone angle. A clear trend emerges: CS displacement tends to increase as the IMF cone angle deviates significantly from 90° —that is, when the IMF has a substantial B_X component. In contrast, when the cone angle is close to 90° , indicating a predominantly cross-flow IMF, the CS displacement remains relatively small.

However, two events deviate from this overall trend. In one case, the cone angle was 99° , yet the intermediate-to-minimum eigenvalue ratio (λ_2/λ_3) was only 1.6, indicating a potentially unreliable determination of the CS normal direction via the MVA. The discrepancy observed in the other case may be attributable to additional influencing factors, such as the potential effects of Martian crustal magnetic fields, which can alter magnetotail structures even after primary crustal influences are excluded (G. A. DiBraccio et al. 2018, 2022; J. Zhou et al. 2024; N. Quartey & M. W. Liemohn 2025). In addition, the event observed on 2016 March 5 exhibits particularly interesting characteristics: the CS normal vector contained a dominant X component, in contrast to the expected alignment within the Y – Z plane. This unusual orientation may

be associated with the radial (tail-aligned) IMF configuration during this event, which can directly distort the CS orientation away from its nominal geometry.

Overall, the analysis of these carefully selected CS crossings supports the existence of a correlation between CS displacement and the IMF cone angle. Specifically, when the cone angle is significantly less than 90° , the CS tends to shift toward the $+Y$ direction (corresponding to the $+B_X$ hemisphere), whereas cone angles significantly greater than 90° are associated with a displacement toward the $-Y$ direction.

5. Statistical Analysis

The analysis of selected CS crossing cases suggests a possible correlation between the CS shifted distance (Δd) and the cone angle of the upstream IMF. However, concerns may arise regarding the potential bias in selecting CS crossing cases, which could undermine the reliability of the results. To address this, it is critical to perform a statistical analysis to examine the effects of the IMF flow-aligned component (B_X) on the average configurations of CS structures in the Martian magnetotail. For this purpose, MAVEN MAG magnetic field data from 2014 October to 2020 February were used.

The statistical analysis was conducted in the Mars-Solar-Electric-field (MSE) coordinate system, which provides a more appropriate frame for studying CS structures (R. Ramstad et al. 2020; C. Zhang et al. 2022; Y. Wen et al. 2025b). This involves a transformation in the Y – Z plane based on the solar wind convection electric field (E_{SW}) calculated using the antisunward solar wind flow (V_{sw}) along the $-X_{\text{MSO}}$ direction and the perpendicular IMF orientation ($\mathbf{B}_{\text{IMF_YZ}}$): $E_{\text{SW}} = -V_{\text{sw}} \times \mathbf{B}_{\text{IMF_YZ}}$. In MSE coordinates, E_{SW} is aligned with the Z_{MSE} axis, while $-V_{\text{sw}}$ and $\mathbf{B}_{\text{IMF_YZ}}$ are aligned with the X_{MSE} and Y_{MSE} axes, respectively. The Z_{MSE} axis lies approximately in the CS plane, which is nominally located near $Y_{\text{MSE}} \sim 0$. Following the procedures used in prior studies (Z. Rong et al. 2014, 2016), orbits were selected where the upstream IMF satisfied the steady-state requirements

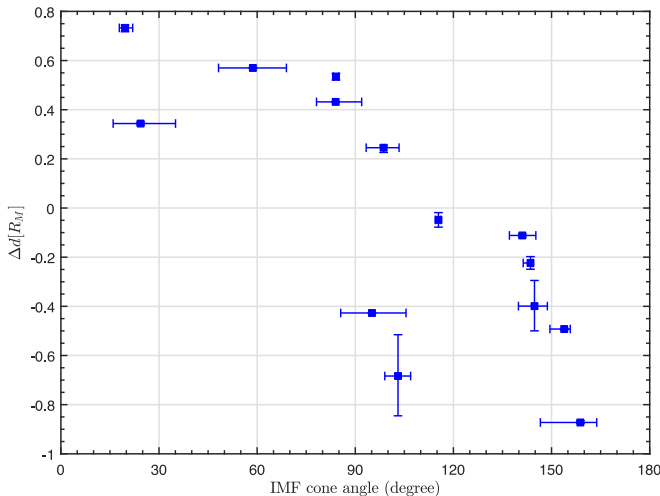


Figure 8. Scatterplot represents the shifted distance of the CS as a function of the IMF cone angle. The lengths of the horizontal error bars represent the IMF cone angle deviation between the IMF for inbound and outbound bow shock crossings. The lengths of the vertical error bars represent the uncertainty of the shifted distance from the uncertainty of the CS normal estimated by the MVA.

defined in Section 4.4. A total of 1445 magnetospheric crossings met these criteria. The MAVEN magnetic field data were then transformed into the MSE coordinate system, constrained to the magnetotail region ($-3R_M < X_{\text{MSE}} < -0.5R_M$). The MSE coordinates were computed using the averaged upstream IMF ($(B_1 + B_2)/2$) and the corresponding solar wind velocity measured by SWIA (J. S. Halekas et al. 2017).

To further validate the robustness of our dataset and analysis framework, we also reproduced the well-known twisted magnetotail structure in the MSO coordinate system under IMF $+B_Y$ and $-B_Y$ conditions, consistent with the findings of G. A. DiBraccio et al. (2018, 2022) (Figure 11 in Appendix A). This reproduction demonstrates that our dataset is capable of recovering previously established results, thereby confirming its reliability. Importantly, when the same dataset is transformed into the MSE system and all IMF cone angles are included, the clear twisted pattern in MSO becomes less apparent, as shown in T. Hara et al. (2022). This allows for a better investigation of the key role of the radial IMF component in governing the global configuration of the Martian magnetotail.

To determine the average CS configuration, the spatial distributions of the B_X component in the MSE Y - Z plane were examined. Spatial bins of size $0.2 \times 0.2 R_M$ were used, and the contours of $B_X = 0$ in this plane were computed to represent the average configuration of the CS structure. To evaluate the effects of the IMF flow-aligned component on the CS configuration, the analysis was conducted under different IMF cone angle conditions: significant sunward IMF (cone angle $< 60^\circ$, 500 magnetospheric crossings), tailward IMF (cone angle $> 120^\circ$, 260 magnetospheric crossings), and cross-flow IMF ($70^\circ < \text{cone angle} < 110^\circ$, 439 magnetospheric crossings). Figure 9 shows the spatial distributions of B_X in MSE coordinates for the three IMF conditions. Figures 9(a), (b), and (c) correspond to sunward, tailward, and cross-flow IMF conditions, respectively. The contours of $B_X = 0$ were automatically generated using MATLAB’s interpolation techniques, which may cause the contours to pass through some spatial bins where $B_X \neq 0$. Additionally, certain “circle

structures” appear in the lobes of the contours. These circles do not have physical significance and are likely artifacts arising from uncertainties in the IMF measurements in specific cases (Z. Rong et al. 2016). It is also worth noting that the number of crossings under tailward IMF conditions (cone angle $> 120^\circ$) is about half that under sunward IMF conditions (cone angle $< 60^\circ$). This imbalance may reflect that the Parker spiral geometry favors smaller cone angles at Mars’ heliocentric distance. Although this results in fewer tailward events and thus larger uncertainties, the main trends identified in the magnetotail CS configuration remain robust.

To assess the influence of crustal magnetic fields, this statistical study compares the average CS configurations under conditions with and without the inclusion of crustal fields. To minimize the impact of the strongest crustal anomalies, magnetic field data recorded by MAVEN in the magnetotail region over the southern hemisphere’s intense crustal field zone were excluded from the analysis. Figures 9(d)–(f) present the average CS configurations under sunward, tailward, and cross-flow IMF orientations when strong crustal magnetic fields are included. Given the limited crustal field spatial effects, we also analyzed their impact in the near-Mars magnetotail using a closer radial distance confinement ($-1.5R_M < X_{\text{MSE}} < -0.5R_M$), as shown in Figure 10.

While the CS structure is often assumed to align with the solar wind motional electric field (E_{SW}), the statistical results indicate that the average CS configurations are highly sensitive to the IMF cone angle, as demonstrated in Figure 8. This finding suggests that the shift of the CS structure is significantly influenced by the cone angle of the IMF. Furthermore, the systematic control of the CS offset in MSE coordinates by the IMF orientation is evident in Figures 9 and 10. Specifically, the CS shifts toward the dusk ($+Y$) direction when the IMF is strongly sunward (cone angle $< 60^\circ$), resulting in the asymmetric magnetotail structure and a dominant $+B_X$ magnetic lobe. Conversely, the CS shifts toward the dawn ($-Y$) direction under tailward IMF conditions (cone angle $> 120^\circ$), corresponding to a dominant $-B_X$ magnetic lobe. Under cross-flow-dominant IMF conditions ($70^\circ < \text{cone angle} < 110^\circ$), the magnetotail lobes are symmetric and the CS is nearly centered around $Y_{\text{MSE}} \sim 0$, with similar results observed in the near-Mars magnetotail region ($-1.5R_M < X_{\text{MSE}} < -0.5R_M$).

Considering the influence of crustal magnetic fields, the general CS configurations remain similar when crustal fields are included, though minor deviations are observed near $Z_{\text{MSE}} \sim 0$ in regions where strong crustal magnetic fields are present. In the near-Mars magnetotail, the average CS configurations exhibit greater variability, with portions of the contours offset when crustal fields are included. These comparisons confirm that crustal magnetic fields can affect CS configurations in the Martian magnetotail (G. A. DiBraccio et al. 2018, 2022). However, the statistical analysis suggests that the flow-aligned component (radial) of the IMF (cone angle) is still the dominating factor responsible for the shift of the CS structure in this case.

It is worth noting that M. W. Liemohn et al. (2017) reported that the asymmetry of the CS may also be influenced by ionospheric conditions, with the CS shifting toward the dawn ($-Y$) during solar maximum and toward the dusk ($+Y$) during solar minimum. Their MHD simulations suggest that this behavior is likely driven by variations in solar EUV intensity.

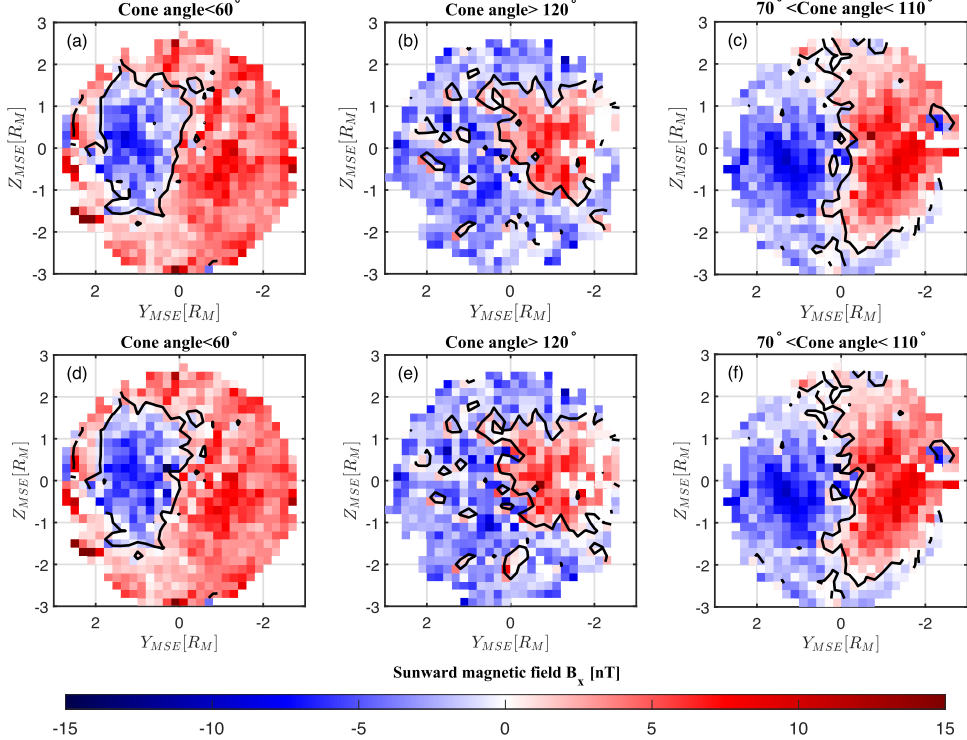


Figure 9. The distribution of the B_x component in the modified Mars-Solar-Electric-field (MSE) coordinates ($-3R_M < X_{MSE} < -0.5R_M$) when the average upstream IMF ($(B_1 + B_2)/2$) is significantly (a) sunward (cone angle $<60^\circ$) and (b) tailward (cone angle $>120^\circ$); (c) cross-flow ($70^\circ < \text{cone angle} < 110^\circ$). The average configurations of the tail current sheet structure are marked by the solid black lines. (a)–(c) represent the current sheet configurations without crustal magnetic field effects. (d)–(f) represent the current sheet configurations with crustal magnetic fields effects.

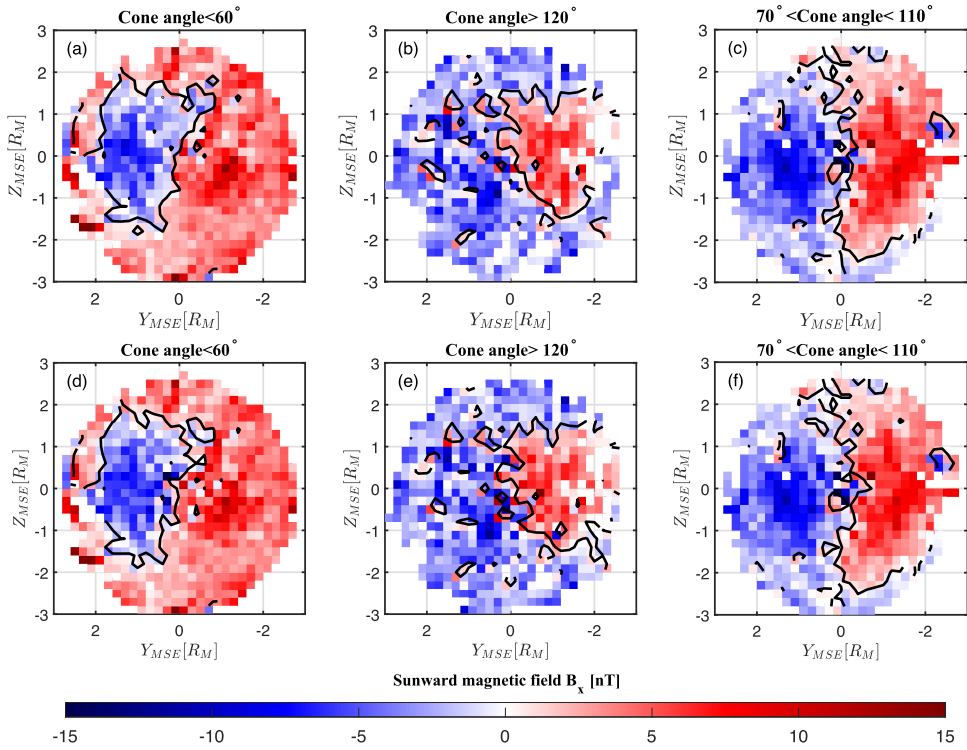


Figure 10. The distribution of the B_x component in the modified Mars-Solar-Electric-field (MSE) coordinates ($-1.5R_M < X_{MSE} < -0.5R_M$) when the average upstream IMF ($(B_1 + B_2)/2$) is significantly (a) sunward (cone angle $<60^\circ$) and (b) tailward (cone angle $>120^\circ$); (c) cross-flow ($70^\circ < \text{cone angle} < 110^\circ$). The average configurations of the tail current sheet structure are marked by the solid black lines. (a)–(c) represent the current sheet configurations without crustal magnetic field effects. (d)–(f) represent the current sheet configurations with crustal magnetic fields effects.

To evaluate the potential influence of solar EUV intensity on the Martian magnetotail structure, we compared magnetic field configurations under varying EUV conditions, including both perihelion and aphelion periods (see Figure 12 in Appendix B). The results indicate that variations in solar EUV intensity do not produce a significant displacement of the tail CS, consistent with recent simulation findings by N. Quartey & M. W. Liemohn (2025). Although minor asymmetries in the magnetic lobes were observed under low EUV conditions, these effects appear limited. The role of ionospheric response in modulating CS displacement under different solar EUV conditions may warrant further investigation in future studies; however, it lies beyond the scope of the present work.

Based on the results above, our statistical analyses support the conclusions drawn from the selected individual cases: the shift of the CS structure and asymmetry of the magnetic lobes in the Martian magnetotail are primarily controlled by the flow-aligned component of the IMF (B_X).

6. Discussion and Conclusions

In this study, we conducted a comprehensive analysis of the Martian magnetotail CS structure using MAVEN magnetic field and plasma data collected between 2014 October and 2020 February. Based on a carefully selected set of CS crossing events, we identified a possible statistical correlation between the displacement of the CS and the flow-aligned component of the IMF (IMF B_X). As illustrated in Figure 8, the CS consistently shifts toward the $-B_X$ hemisphere under sunward IMF conditions and toward the $+B_X$ hemisphere under tailward IMF conditions. In contrast, cross-flow-dominated IMF configurations produce minimal CS displacement, consistent with results of previous studies (N. Romanelli et al. 2014; Y. Li et al. 2021; G. Li et al. 2023).

Further support for this conclusion is provided by statistical averages of CS configurations under different IMF orientations in modified MSE coordinates (Figures 9 and 10). Under strong IMF B_X conditions, the magnetic lobes become asymmetric, and the CS is significantly displaced from the center. In contrast, when the IMF B_X component is weak or negligible, the magnetotail remains largely symmetric. These results reveal the dominant influence of the flow-aligned IMF component in shaping the geometry of the Martian tail CS. To isolate the potential influence of the IMF orientation from other contributing factors, we further examined the structure of the tail CS while accounting for the potential effects of crustal magnetic fields and variations in solar EUV intensity (G. A. DiBraccio et al. 2018; M. W. Liemohn et al. 2017). The analysis confirms that the IMF B_X component plays an important role in the observed CS displacement in the magnetotail. Recent MHD simulations by G. Li et al. (2023) also demonstrate that variations in IMF orientation—specifically changes in the Parker spiral angle—significantly influence the structure of the Martian magnetotail. Their results show that as the IMF becomes increasingly aligned with the solar wind flow (stronger radial IMF component), the Martian magnetotail develops a pronounced dawn–dusk asymmetry in the lobe structure, with the dawn-side lobe contracting and the dusk-side expanding. More importantly, the position of the CS and the IPRL shifts away from the equator, migrating systematically toward the dawn side. These simulation results are consistent with our observational findings by MAVEN. The physical mechanism inferred from

G. Li et al. (2023) centers on the asymmetric draping and magnetic pressure distribution introduced by the IMF B_X . As the IMF becomes more flow-aligned, it enters the magnetosheath at a shallower angle, producing a less symmetric configuration as the field lines drape around the planet. This asymmetric draping results in a differential magnetic pressure between the dawn and dusk lobes, with weaker pressure and more flared field lines on the dawn side. Consequently, the magnetic lobes become structurally imbalanced, and the CS shifts toward the region of lower magnetic pressure. Notably, this interpretation from the simulation is similar to the mechanism proposed by D. J. McComas et al. (1986) for the asymmetry of the Venusian magnetotail observed by PVO.

Nevertheless, some differences compared to previous studies may require further discussion. In particular, despite using a similar analytical approach, Z. Rong et al. (2016) reported no clear correlation between the IMF B_X component and magnetic field asymmetries in the near-Venus magnetotail using VEX observations. Their results contrast with those of D. J. McComas et al. (1986), who observed IMF-driven asymmetries at Venus. Z. Rong et al. (2016) offered two possible explanations for this discrepancy (see their Discussion and Conclusion): (1) the observed asymmetry may arise from other unknown factors, such as the biased PVO data set, which included limited upstream solar wind and IMF measurements; and (2) while the IMF B_X may influence the magnetic field structure, its effect may not be significant in the near-Venus magnetotail region where VEX observations were conducted. Additionally, Z. Rong et al. (2016) referenced the theoretical work by N. Romanelli et al. (2014), which, based on an analytical model, concluded that only the cross-flow component of the IMF significantly contributes to shaping the magnetotail; the flow-aligned component B_X does not displace the tail CS. This is consistent with their observational results. However, nonideal MHD and hybrid simulation studies (E. Kallio et al. 2006; Y. Ma et al. 2013; S. Simon & U. Motschmann 2009) have shown that when particle effects such as resistivity and collisions are included, the IMF B_X can indeed lead to a displacement of the tail CS, aligning with the observations reported by D. J. McComas et al. (1986) and S. Simon et al. (2013). Based on this contrast, Z. Rong et al. (2016) made the argument that although resistivity and particle effects may facilitate CS displacement by IMF B_X in simulations, they do not appear to play a dominant role in the formation of the near-Venus magnetotail, as indicated by VEX observations. However, the exact physical mechanism behind the inconsistency remains unclear; therefore, further detailed investigations are necessary to clarify the role of IMF B_X in the structure and dynamics of the Venus magnetotail.

These different features observed on the magnetotail of Mars and Venus may imply that the penetration depth and impact of IMF B_X may be sensitive to plasma conditions on different planets. Mars, with its weaker ionospheric shielding, substantial mass loading, and nonuniform magnetic topology (due to crustal fields; S. Xu et al. 2019, 2020; J. Qin et al. 2025), may be more permissive to magnetic field restructuring by the upstream IMF (C. Fowler et al. 2019; S. Byrd et al. 2024; J. Gao et al. 2024). Venus, on the other hand, presents a more effective and uniform barrier to such restructuring in the near-tail, likely preserving a symmetric tail geometry that aligns more with ideal MHD predictions in this region based on observations by Z. Rong et al. (2016). This comparative

analysis may imply that different plasma environments could potentially be a crucial determinant in shaping the distinct features of the induced magnetotails of unmagnetized planets. Continued and future exploration at Venus is essential to deepen our understanding of how different plasma environments at Mars and Venus govern their respective solar wind interactions (E. Dubinin & M. Fraenz 2015). Furthermore, given the variability of the upstream solar wind conditions (D. Liu et al. 2021), coordinated multipoint observations using existing platforms, such as MAVEN and Tianwen-1 (Y. Zou et al. 2021), are crucial for capturing the dynamic response of the induced magnetosphere to changing IMF conditions and transient solar wind events (B. Sánchez-Cano et al. 2022; Y. Wen et al. 2022, 2025a, 2025b; H.-W. Shen et al. 2024; L. Liu et al. 2025; M. Wang et al. 2025). Notably, recent studies have also implied the significant role of the IMF cone angle, particularly under radial IMF conditions, in shaping the induced magnetosphere (C. M. Fowler et al. 2022; Q. Zhang et al. 2024). Multipoint measurements will offer a valuable opportunity to examine these effects with higher spatial and temporal resolution. These efforts will not only improve our understanding of Mars–Venus differences but also help build a broader framework for solar wind–planet interactions across the solar system.

Acknowledgments

The research described in this paper utilizes publicly available data from the MAVEN Science Data Center (<https://lasp.colorado.edu/maven/sdc/public/data/sci/>) and

NASA Planetary Data System (<https://pds-ppi.igpp.ucla.edu/>), including data from the MAG (J. E. P. Connerney 2024), STATIC (J. P. McFadden 2024), SWIA (J. S. Halekas 2024), and SWEA (D. L. Mitchell 2024) instruments. We acknowledge Prof. Jasper S. Halekas for helpful discussions on this work. We also thank the anonymous reviewer for constructive suggestions that improved the manuscript. No MAVEN or NASA funding was utilized to support the conduct of this study.

Author Contributions

Yuanzheg Wen: writing—original draft, visualization, investigation, formal analysis; Zhaojin Rong: conceptualization, writing—review and editing, funding acquisition; Hans Nilsson: writing—review and editing; Chi Zhang: writing—review and editing; Han-Wen Shen: writing—review and editing; Jiawei Gao: writing—review and editing.

Software: IRFU-MATLAB (Y. Khotyaintsev et al. 2024), SPEDAS (V. Angelopoulos et al. 2019).

Appendix A The Twisting Structure of the Magnetotail

Figure 11 shows the average sunward magnetic-field component (B_x) in the Martian magnetotail for $+B_Y$ (a) and $-B_Y$ (b) IMF conditions. The maps, in Y_{MSO} – Z_{MSO} coordinates, reveal opposite lobe polarities, indicating that the tail magnetic configuration reverses with the IMF B_Y direction, consistent with G. A. DiBraccio et al. (2022).

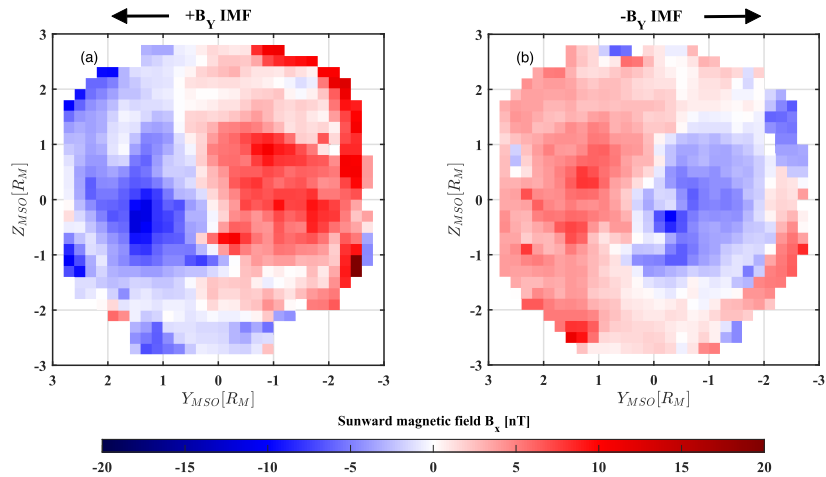


Figure 11. Magnetic maps of the average B_x component in the Martian magnetotail, separated $+B_Y$ IMF (a) and $-B_Y$ (b) conditions in the same format as G. A. DiBraccio et al. (2022).

Appendix B Effects from Solar Extreme-ultraviolet

We utilize measurements from the Extreme Ultraviolet Monitor (EUVM; F. Eparvier et al. 2015) onboard MAVEN to investigate the potential influence of solar EUV flux on the displacement of the Martian magnetotail CS, as suggested by M. W. Liemohn et al. (2017). The MAVEN EUVM includes three channels: Channel A (17–22 nm), Channel B (0.1–7 nm), and Channel C (121–122 nm). Following previous studies such as Y. Dong et al. (2017), we use data from Channel A to represent the level of solar EUV radiation. The magnetic field distribution and CS structure under different EUV conditions are presented in Figure 12.

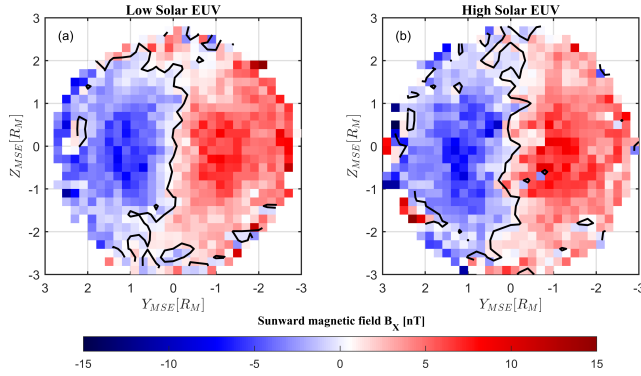


Figure 12. The distribution of the B_x component in the modified Mars-Solar-Electric field (MSE) coordinates under high and low solar EUV conditions.

ORCID iDs

- Yuanzheng Wen <https://orcid.org/0000-0001-6141-6171>
 Zhaojin Rong <https://orcid.org/0000-0003-4609-4519>
 Hans Nilsson <https://orcid.org/0000-0002-7787-2160>
 Chi Zhang <https://orcid.org/0000-0001-9154-596X>
 Han-Wen Shen <https://orcid.org/0000-0001-6733-5065>
 Jiawei Gao <https://orcid.org/0000-0003-4432-1132>

References

- Acuna, M., Connerney, J., Ness, et al. 1999, *Sci*, **284**, 790
 Angelopoulos, V., Cruce, P., Drozdov, A., et al. 2019, *SSRV*, **215**, 1
 Bertucci, C., Duru, F., Edberg, N., et al. 2011, *SSRV*, **162**, 113
 Brain, D. A., Bagenal, F., Acuña, M. H., & Connerney, J. E. P. 2003, *JGRA*, **108**, 1424
 Brain, D. A., Barabash, S., Bouger, S. W., et al. 2017, *The Atmosphere and Climate of Mars* (Cambridge: Cambridge Univ. Press), 464
 Byrd, S., Girazian, Z., & Ruhunusiri, S. 2024, *JGRA*, **129**, e2023JA032343
 Connerney, J., Espley, J., Lawton, P., et al. 2015, *SSRV*, **195**, 257
 Connerney, J. E. P. 2024, *PDSS*
 DiBraccio, G. A., Dann, J., Espley, J. R., et al. 2017, *JGRA*, **122**, 4308
 DiBraccio, G. A., Espley, J. R., Gruesbeck, J. R., et al. 2015, *GeoRL*, **42**, 8828
 DiBraccio, G. A., Luhmann, J. G., Curry, S. M., et al. 2018, *GeoRL*, **45**, 4559
 DiBraccio, G. A., Romanelli, N., Bowers, C. F., et al. 2022, *GeoRL*, **49**, e2022GL098007
 Ding, Y., & Rong, Z. 2018, *ChJG*, **61**, 411
 Dong, Y., Fang, X., Brain, D., et al. 2015, *GeoRL*, **42**, 8942
 Dong, Y., Fang, X., Brain, D., et al. 2017, *JGRA*, **122**, 4009
 Dubinin, E., & Fraenz, M. 2015, *Magnetotails in the Solar System* (New York: Wiley), 43
 Dubinin, E., Fraenz, M., Pätzold, M., et al. 2023, *JGRA*, **128**, e2022JA030575
 Dubinin, E., Fraenz, M., Woch, J., et al. 2012, *GeoRL*, **39**, L01104
 Eparvier, F., Chamberlin, P., Woods, T., & Thiemann, E. 2015, *SSRV*, **195**, 293
 Fowler, C., McFadden, J., Hanley, K., et al. 2022, *JGRA*, **127**, e2022JA030352
 Fowler, C., Lee, C., Xu, S., et al. 2019, *JGRA*, **124**, 3021
 Fowler, C. M., Hanley, K. G., McFadden, J., et al. 2022, *JGRA*, **127**, e2022JA030726
 Fruchtman, J., Halekas, J., Gruesbeck, J., Mitchell, D., & Mazelle, C. 2023, *JGRA*, **128**, e2023JA031759
 Gao, J., Rong, Z., Klinger, L., et al. 2021, *E&SS*, **8**, e2021EA001860
 Gao, J., Rong, Z., Zhang, Q., et al. 2024, *E&PP*, **8**, 728
 Halekas, J. S. 2024, *PDSS*
 Halekas, J. S., Brain, D. A., Lillis, R. J., et al. 2006, *GeoRL*, **33**, L13101
 Halekas, J. S., Luhmann, J. G., Dubinin, E., & Ma, Y. 2021, *Induced Magnetospheres: Mars, Magnetospheres in the Solar System* (New York: Wiley), 391
 Halekas, J. S., McFadden, J. P., Brain, D. A., et al. 2018, *JGRA*, **123**, 8439
 Halekas, J. S., Ruhunusiri, S., Harada, Y., et al. 2017, *JGRA*, **122**, 547
 Halekas, J. S., Taylor, E. R., Dalton, G., et al. 2015, *SSRV*, **195**, 125
 Hanley, K. G., McFadden, J. P., Mitchell, D. L., et al. 2021, *JGRA*, **126**, e2021JA029531
 Hara, T., Huang, Z., Mitchell, D. L., et al. 2022, *JGRA*, **127**, e2021JA029867
 Harada, Y., Halekas, J., DiBraccio, G., et al. 2018, *GeoRL*, **45**, 4550
 Jakosky, B. M., Lin, R. P., Grebowsky, J. M., et al. 2015, *SSRV*, **195**, 3
 Kallio, E., Jarvinen, R., & Janhunen, P. 2006, *P&SS*, **54**, 1472
 Khotyaintsev, Y., Nilsson, T., Johansson, E. P. G., et al. 2024, *IRFU-Matlab* v1.17.0, Zenodo, doi:[10.5281/zenodo.1452504](https://doi.org/10.5281/zenodo.1452504)
 Li, G., Lu, H., Cao, J., Li, Y., & Li, S. 2023, *A&A*, **673**, A3
 Li, X., Rong, Z., Fraenz, M., et al. 2023, *GeoRL*, **50**, e2022GL102630
 Li, Y., Lu, H., Cao, J., et al. 2021, *ApJ*, **921**, 139
 Liemohn, M. W., & Xu, S. 2018, *Electric Currents in Geospace and Beyond* (Washington, DC: AGU), 177
 Liemohn, M. W., Xu, S., Dong, C., et al. 2017, *JGRA*, **122**, 6397
 Liu, D., Rong, Z., Gao, J., et al. 2021, *ApJ*, **911**, 113
 Liu, L., Qiu, X., Yu, Y., et al. 2025, *ApJ*, **983**, 102
 Ma, Y., Nagy, A., Russell, C., et al. 2013, *JGRA*, **118**, 321
 Ma, Y., Nagy, A. F., Hansen, K. C., et al. 2002, *JGRA*, **107**, 1282
 McComas, D. J., Spence, H. E., Russell, C., & Saunders, M. 1986, *JGR*, **91**, 7939
 McFadden, J., Kortmann, O., Curtis, D., et al. 2015, *SSRV*, **195**, 199
 McFadden, J. P. 2024, *PDSS*
 Mitchell, D., Mazelle, C., Sauvad, J.-A., et al. 2016, *SSRV*, **200**, 495
 Mitchell, D. L. 2024, *PDSS*
 Nagy, A., Winterhalter, D., Sauer, K., et al. 2004, *SSRV*, **111**, 33
 Nilsson, H., Carlsson, E., Brain, D. A., et al. 2010, *Icar*, **206**, 40
 Qin, J., Curry, S., Xu, S., et al. 2025, *GeoRL*, **52**, e2025GL116552
 Quartey, N., & Liemohn, M. W. 2025, *JGRA*, **130**, e2024JA033445
 Ramstad, R., Brain, D. A., Dong, Y., et al. 2020, *NatAs*, **4**, 979
 Romanelli, N., Bertucci, C., Gómez, D., & Mazelle, C. 2015, *JGRA*, **120**, 7737
 Romanelli, N., Gómez, D., Bertucci, C., & Delva, M. 2014, *ApJ*, **789**, 43
 Rong, Z., Barabash, S., Futaana, Y., et al. 2014, *JGRA*, **119**, 8838
 Rong, Z., Barabash, S., Stenberg, G., et al. 2015a, *JGRA*, **120**, 3462
 Rong, Z., Barabash, S., Stenberg, G., et al. 2015b, *JGRA*, **120**, 5593
 Rong, Z., Stenberg, G., Wei, Y., et al. 2016, *JGRA*, **121**, 10
 Sánchez-Cano, B., Lester, M., Andrews, D. J., et al. 2022, *ExA*, **54**, 641
 Shen, H.-W., Halekas, J. S., Curry, S. M., et al. 2025, *ApJ*, **990**, 115
 Shen, H.-W., Halekas, J. S., McFadden, J. P., Gruesbeck, J. R., & Schnepf, N. R. 2024, *ApJ*, **975**, 175
 Simon, S., & Motschmann, U. 2009, *P&SS*, **57**, 2001
 Simon, S., van Treec, S. C., Wennmacher, A., et al. 2013, *JGRA*, **118**, 1679
 Sonnerup, B. U. 1998, *Analysis Methods for Multi-spacecraft Data*, Vol. 1 (Paris: ESA/ISSI), 185
 Vignes, D., Mazelle, C., Rme, H., et al. 2000, *GeoRL*, **27**, 49
 Wang, M., Zhang, J., Lu, J., et al. 2025, *GeoRL*, **52**, e2024GL112219
 Wen, Y. 2025, MAVEN Bow Shock Crossing List from Nov 2014 to Feb 2020 v1, Zenodo, doi:[10.5281/zenodo.15881610](https://doi.org/10.5281/zenodo.15881610)
 Wen, Y., Halekas, J. S., Shen, H.-W., et al. 2025b, *ApJL*, **982**, L42
 Wen, Y., Halekas, J. S., Shen, H.-W., et al. 2025a, ESS Open Archive, **10**, 22541/essoar.176126722.22353060/v1
 Wen, Y., Tao, D., Wang, G., et al. 2022, *E&PP*, **6**, 313
 Xu, S., Mitchell, D. L., Weber, T., et al. 2020, *JGRA*, **125**, e2019JA027755
 Xu, S., Weber, T., Mitchell, D. L., et al. 2019, *JGRA*, **124**, 1823
 Zhang, C., Dong, C., Zhou, H., et al. 2025, *GeoRL*, **52**, e2024GL113030
 Zhang, C., Rong, Z., Klinger, L., et al. 2022, *JGRE*, **127**, e2022JE007334
 Zhang, C., Rong, Z., Li, X., et al. 2024, *GeoRL*, **51**, e2023GL107190
 Zhang, C., Rong, Z., Zhang, L., et al. 2023, *JGRA*, **128**, e2022JA031232
 Zhang, Q., Barabash, S., Holmstrom, M., et al. 2024, *Natur*, **634**, 45
 Zhou, J., Liu, K., Jarvinen, R., et al. 2024, *ApJ*, **976**, 7
 Zou, Y., Zhu, Y., Bai, Y., et al. 2021, *AdSpR*, **67**, 812